

# Asymmetric Metal-Dielectric Metacylinders and Their Potential Applications From Engineering Scattering Patterns to Spatial Optical Signal Processing


Ali Momeni,<sup>1</sup> Mahdi Safari,<sup>2</sup> Ali Abdolali,<sup>3</sup> Nazir P. Kherani,<sup>2,4</sup> and Romain Fleury<sup>1,\*</sup>

<sup>1</sup>*Laboratory of Wave Engineering, Swiss Federal Institute of Technology in Lausanne (EPFL), Lausanne CH-1015, Switzerland*

<sup>2</sup>*Department of Electrical and Computer Engineering, University of Toronto, 10 King's College Road, Toronto M5S 3G4, Canada*

<sup>3</sup>*Applied Electromagnetic Laboratory, School of Electrical Engineering, Iran University of Science and Technology, Narmak, Tehran, Iran*

<sup>4</sup>*Department of Materials Science and Engineering, University of Toronto, 140 College Street, Toronto, Ontario M5S 3E4, Canada*

 (Received 24 August 2020; revised 15 January 2021; accepted 29 January 2021; published 3 March 2021)

We propose a bianisotropic hybrid metal-dielectric structure comprising dielectric and metallic cylindrical wedges wherein the composite metacylinder enables advanced control of electric, magnetic, and magnetoelectric resonances. We establish a theoretical framework in which the electromagnetic response of this meta-atom is described through the electric and magnetic multipole moments. The complete dynamic polarizability tensor, expressed in a compact form, is derived as a function of the Mie-scattering coefficients. Further, the constitutive parameters—determined analytically—illustrate the tunability of the structure's frequency and strength of resonances in light of its high degree of geometric freedom. Flexibility in the design makes the proposed metacylinder a viable candidate for various applications in the microscopic (single meta-atom) and macroscopic (metasurface) levels. We show that the highly versatile bianisotropic meta-atom is amenable to being designed for the desired electromagnetic response, such as electric dipole-free and zero or near-zero (backward and forward) scattering at the microscopic level. In addition, we show that the azimuthal asymmetry gives rise to normal polarizability components, which are vital elements in synthesizing asymmetric optical transfer function at the macroscopic level. We conduct a precise inspection, from the microscopic to the macroscopic level, of the metasurface synthesis for emphasizing on the role of normal polarizability components for spatial optical signal processing. It is shown that this simple two-dimensional asymmetric meta-atom can perform first-order differentiation and edge detection at normal illumination. The results reported herein contribute toward improving the physical understanding of wave interaction with artificial materials composed of asymmetric elongated metal-dielectric inclusions and open the potential of its application in spatial signal and image processing.

DOI: [10.1103/PhysRevApplied.15.034010](https://doi.org/10.1103/PhysRevApplied.15.034010)

## I. INTRODUCTION

Modeling of two-dimensional structures illuminated by electromagnetic waves has been of leading research interest for a long time. The problem of deriving the polarization of elongated structures has been of central interest in the study of antenna theory over the last century [1]. Due to their simplicity and practicality, long metallic and dielectric cylinders and wire media structures have received much attention among all the various canonical 2D structures. These include structures realizing artificial plasmas [2], hyperbolic media [3–6], creating exotic material properties [7–12], including those for antenna applications

[13,14], tailoring the phase of reflection waves in metasurface applications [15–23], imaging and endoscopy [24–26], manipulating Casimir forces [27], enhancing the coupling to quantum sources [28–30] and enabling single-molecule biosensors [31].

The first fundamental step to describing the electromagnetic (EM) response of a metamaterial is to model the response of an individual particle. In this method each inclusion serves as a polarizable particle, which is modeled with a pair of electromagnetic polarizable dipoles, which in turn becomes a new source of electromagnetic fields that lead to corresponding local fields. Ultimately, these effects form the macroscopic constitutive parameters. Unusual properties of this material are observed near resonance and its dependence on the geometry and

\*romain.fleury@epfl.ch

EM properties of the individual inclusions are self-evident [32]. A number of recent studies retrieve the EM response for elongated cylinders under specific conditions of incidence, such as normal incidence [32]. For example, static expressions for the transverse polarizability components of circular cylinders are well established, and recently have been extended to the dynamic case based on far-field scattering considerations [33]. However, because of symmetry restrictions of the infinitely long cylinder, this particle does not possess any magnetoelectric coupling response at normal incidences. In general, no magnetoelectric coupling may exist in the microscopic polarizability of a scatterer with both temporal and inversion symmetry [34,35]. Most structures proposed so far in this area act only as a symmetric system, which gives almost no flexibility for controlling the scattering patterns. Considering the inability of these symmetric meta-atoms, exploring an asymmetric meta-atom with different geometrical parameters is of high relevance. In addition, it should be noted that various nanoparticles with a large number of degrees of freedom are reported in the literature [36–40]. However, all these meta-atoms are designed using heavy computational tools, which is a time-consuming approach that brings much less physical insight than the type of analytical modeling proposed here. We believe that an analytical path to the full dynamic polarizability tensor is useful as it enables advanced control of electric, magnetic, and magnetoelectric resonances directly, and readily provides physical insight prior to the design procedure. Therefore, the extraction of full polarizability tensors for such a complex meta-atom [41,42] is of high interest and has application ranging from computational metasurfaces to transparency and invisibility.

More recently, wave-based analog computing with metamaterial has attracted tremendous attention, in which material-based computing elements have been explored to efficiently manipulate the optical wave front in the wave-vector domain [43]. The advantage of material-based analog computing over the conventional electronic systems for analog computing and signal processing are as follows; lower energy consumption, and lower computational time [44,45]. Over the past few years, several metamaterial and metasurface-based computational devices have been reported in the optical analog computing realm [46–56]. Metasurface-based processors are proposed to mitigate the drawbacks associated with the Fourier transform sub-blocks, such as topological analog signal processing [57], photonic crystals [58], and all-dielectric metasurfaces [51,59,60].

Here, we introduce the metal-dielectric “metacylinder” as an asymmetric meta-atom with a tunable wedge angle presenting high degrees of design freedom. We firstly analyze the metal-dielectric metacylinder with large degrees of freedom, and thereafter we derive the full dynamic polarizability tensors describing the

electromagnetic response of the proposed meta-atom. Breaking azimuthal symmetry can result in an unconventional scattering pattern and unbalanced radiation power, which also can be useful for tailoring the transverse optical forces. The fact that asymmetrical structures arise excitation of normal polarizability tensor components (i.e., towards the direction of illumination), opens up possibilities for pursuing different applications such as beam deflection and advanced analog computing [49,50,61], where designing and realizing a metasurface processor with an asymmetrical optical transfer function (OTF) capable of distinguishing and separating the  $k_x$  and  $-k_x$  at normal incident is one of the main challenges of this field [47,49,50,53,62]. To demonstrate the ability of the asymmetrical metal-dielectric metacylinder as an adjustable 2D meta-atom, we utilize the proposed meta-atom to address the recent challenges of the field of wave engineering and signal processing. The optical performance of the proposed meta-atom at both single meta-atom and metasurface levels is explored, in which near-zero scattering achieved from a single meta-atom showing its viability for invisible sensors and transparent metamaterial applications and a metasurface comprising an array of metacylinder is proposed for signal and image processing. A metasurface processor consisting of the proposed meta-atom is realized, which is well capable of performing mathematical operations such as first-order differentiation operation, edge detection of an arbitrary input signal.

## II. SCATTERING ANALYSIS OF A METAL-DIELECTRIC METACYLINDER

The configuration of the structure and illumination is shown in Fig. 1. The presented meta-atom consists of two finite wedges, which together form a complete cylinder. The material properties for these wedges are different, one is a metal and the other is a dielectric where  $\epsilon_c$  and  $\mu_c$  are its permittivity and permeability, respectively.

$r_0$  is the radii of the structure and  $\beta$  is the metal wedge angle. In order to solve the 2D problem in the most general manner, we consider the incident wave to impinge upon the structure at different azimuthal angles. This is achieved by fixing the incident wave while rotating the structure to the desired angle ( $\alpha$ ) (see Fig. 1). It is noteworthy that in this study we assume the time dependence to be  $e^{-j\omega t}$ .

Considering that the structure is of infinite extent along the longitudinal axis it is clear that  $\partial F/\partial z = 0$ , where  $F$  represent all the EM parameters. Given that the problem of EM scattering from a finite perfect electric conductor (PEC) wedge has been solved previously for TE and TM polarizations [63], here we extend the structure by filling in the remaining part of the cylinder with a dielectric and thus enabling the analysis to simply avail the same scattering

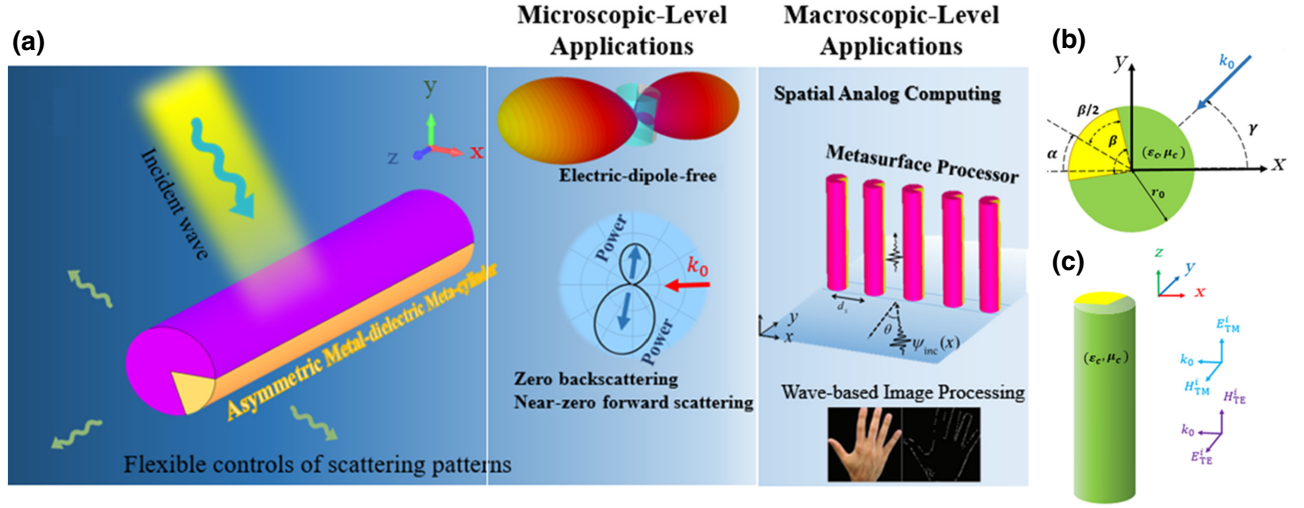


FIG. 1. (a) Schematic sketch of the proposed bianisotropic meta-atom and its microscopic and macroscopic-level applications. (b) two-dimensional (2D) view, and (c) three-dimensional (3D) view of meta-atom orientation.

wave forms.

$$E_{z,sc}^{TM} = \sum_{n=0}^{\infty} \left\{ a_n^{TM} \cos[n(\varphi + \alpha)] + b_n^{TM} \sin[n(\varphi + \alpha)] \right\} H_n^{(1)}(k_0 r), \quad (1)$$

$$H_{z,sc}^{TE} = \sum_{n=0}^{\infty} \left\{ a_n^{TE} \cos[n(\varphi + \alpha)] + b_n^{TE} \sin[n(\varphi + \alpha)] \right\} H_n^{(1)}(k_0 r), \quad (2)$$

where  $E_{z,sc}^{TM}$  and  $H_{z,sc}^{TE}$  are the electric and magnetic field components along the  $z$  axis describing the TM and TE polarizations, respectively.  $k_0 = \omega\sqrt{\epsilon_0\mu_0}$  denotes the wave number in free space and  $\alpha$  is the orientation angle of the metacylinder. It is worth noting that the preceding equations are derived using the EM boundary conditions, in which the  $a_n$  and  $b_n$  are the Mie-scattering coefficients. A detailed derivation of the aforementioned equations is outlined in Appendices A and B. Assuming that the radius of the meta-atom is smaller than the wavelength, the higher-order modes can be neglected leaving the dominant first-order terms. Hence, replacing the Hankel functions with its far-field approximation simplifies the scattering wave expression as shown below.

$$E_z^{TM, far} = \sqrt{\frac{2}{\pi k_0 r}} \left\{ a_0^{TM} + \left[ a_1^{TM} \cos(\alpha) + b_1^{TM} \sin(\alpha) \right] \cos(\varphi) \right.$$

$$\left. + \left[ b_1^{TM} \cos(\alpha) - a_1^{TM} \sin(\alpha) \right] \sin(\varphi) \right\} \exp \left[ j(k_0 r - \pi/4) \right], \quad (3)$$

$$H_z^{TE, far} = \sqrt{\frac{2}{\pi k_0 r}} \left\{ a_0^{TE} + \left[ a_1^{TE} \cos(\alpha) + b_1^{TE} \sin(\alpha) \right] \cos(\varphi) \right.$$

$$\left. + \left[ b_1^{TE} \cos(\alpha) - a_1^{TE} \sin(\alpha) \right] \sin(\varphi) \right\} \times \exp \left[ j(k_0 r - \pi/4) \right]. \quad (4)$$

For the thin metal-dielectric metacylinder, which are of interest here, scattering is dominated by the  $n = 0$  and 1 in TM and TE harmonics, that obviously depend on the incident polarization, the geometric ( $\alpha$  and  $\beta$  angles and  $r_0$ ) and constitutive parameters ( $\epsilon_c = \epsilon_r \epsilon_0$  and  $\mu_c = \mu_r \mu_0$  of dielectric wedge).

### III. DYNAMIC POLARIZABILITY TENSOR EXTRACTION

Modeling of the electromagnetic fields using multipole moments has several advantages. The electromagnetic fields are linearly dependent on the moments and as a result do not involve complicated integrals [32]. The resulting multiple moments are vital elements in the description of homogeneous effective medium theories such as Maxwell-Garnet and other nonlocal methods [26,64]. In the following sections, we first derive the analytical expression for

the induced electric and magnetic dipoles based on the multiple moments' theory. Next, we extract the polarizability tensors using the standing-wave approach, which describe the EM interaction of the proposed structure.

### A. Extraction of multipole moments

The radiated fields due to a set of electric and magnetic dipoles can be approximately expressed as presented by [65]

$$\vec{E} \simeq Z_0 \left\{ [k_0^2 \vec{p} c_0 G + (\vec{p} c_0 \cdot \nabla) \nabla G] + j k_0 [\nabla G \times \vec{m}] \right\}, \quad (5)$$

$$\vec{H} \simeq -j k_0 [\nabla G \times \vec{p} c_0] + [k_0^2 \vec{m} G + (\vec{m} \cdot \nabla) \nabla G], \quad (6)$$

where  $k_0$ ,  $c_0$  are the wave vector and the speed of light, respectively.  $\nabla = \hat{r}(\partial/\partial r)$  ( $\hat{r}$  is a cylindrical unit vector along the radial direction). Here, we are going to derive the induced electric and magnetic dipole moments in a 2D structure. Consequently, we can use the 2D cylindrical Green function  $G = (j/4)H_0^{(1)}(k_0 r)$  as an alternative. As a result, we utilize the analytical expression for the electromagnetic radiation of electric and magnetic dipole moments wherein the radiated fields are expressed as TE and TM modes [32] using far-field approximation.

$$\vec{E}_{\text{TM}}^{\text{far}} = \hat{z} \frac{j Z_0 k_0^2}{4} \sqrt{\frac{2}{\pi k_0 r}} (p_z c_0 - 2m_\phi) \exp \left[ j(k_0 r - \pi/4) \right], \quad (7)$$

$$\vec{H}_{\text{TM}}^{\text{far}} = -\frac{j k_0^2}{4} \hat{\phi} (p_z c_0 - 2m_\phi) \exp \left[ j(k_0 r - \pi/4) \right], \quad (8)$$

$$\vec{E}_{\text{TE}}^{\text{far}} = \hat{\phi} \frac{j Z_0 k_0^2}{4} \sqrt{\frac{2}{\pi k_0 r}} (p_\phi c_0 + m_z) \exp \left[ j(k_0 r - \pi/4) \right], \quad (9)$$

$$\vec{H}_{\text{TE}}^{\text{far}} = \frac{j k_0^2}{4} \hat{z} (p_\phi c_0 + m_z) \exp \left[ j(k_0 r - \pi/4) \right]. \quad (10)$$

It is noteworthy that  $p_\phi$  and  $m_\phi$  describe projections of the moments along the azimuthal direction ( $p_\phi = p_y \cos \phi - p_x \sin \phi$ ,  $m_\phi = m_y \cos \phi - m_x \sin \phi$ ) and should not be confused with the azimuthal components since the dipoles  $\mathbf{P}$  and  $\mathbf{M}$  are located at the origin of the axes. Observing the above equations, it is clear that the radiating fields correspond to typical cylindrical TEM waves, satisfying  $\vec{H} = \hat{n} \times E/Z_0$ . The dipole moments excited in the metal-dielectric metacylinder can now be derived using

the approach presented in Ref. [32]. First, we analytically extract the far-field scattering TE and TM fields for the metal-dielectric metacylinder (see Sec. II), and then we derive the far-field radiation due to the set of electric and magnetic dipoles [Eqs. (12) to (15)]. Thereafter, we extract the induced dipole moments by comparing Eqs. (3) and (4) and Eqs. (12) to (15). The relation between the Mie coefficients and the induced dipole moments is derived:

$$P = -\hat{x} \frac{4 \left[ b_1^{\text{TE}} \cos(\alpha) - a_1^{\text{TE}} \sin(\alpha) \right]}{j k_0^2 c_0} + \hat{y} \frac{4 \left[ a_1^{\text{TE}} \cos(\alpha) + b_1^{\text{TE}} \sin(\alpha) \right]}{j k_0^2 c_0} + \hat{z} \frac{4 a_0^{\text{TM}}}{j k_0^2 Z_0 c_0}, \quad (11)$$

$$M = \hat{x} \frac{2 \left[ b_1^{\text{TM}} \cos(\alpha) - a_1^{\text{TM}} \sin(\alpha) \right]}{j k_0^2 Z_0} - \hat{y} \frac{2 \left[ a_1^{\text{TM}} \cos(\alpha) + b_1^{\text{TM}} \sin(\alpha) \right]}{j k_0^2 Z_0} + \hat{z} \frac{4 a_0^{\text{TE}}}{j k_0^2}. \quad (12)$$

Upon observation of the equations, it is clear that the extracted dipole moments can be easily tuned by varying the angular rotation  $\alpha$  and the scattering Mie coefficients by changing the wedge angle  $\beta$ . In order to verify the validity of our approach, we derive using full-wave simulations (i.e., CST Microwave Studio) the far-field scattering pattern of a metal-dielectric metacylinder comprising a dielectric with a relative permittivity of  $\epsilon_r = 18$  and gold as the metal component with conductivity  $\sigma = 4.561 \cdot 10^7$  S/m and a wedge angle of  $\pi$ . We also extract the radiation of the induced dipole moments, and also the closed-form Mie scattering of the metal-dielectric metacylinder (Sec. II). The incident wave is assumed to be a TM plane wave with the operating wave length of  $\lambda_0 = 6 \mu\text{m}$ . Figure 2 presents the mentioned results for three metal-dielectric cylinders with different radii's 600 nm, 800 nm, and 1  $\mu\text{m}$ , respectively. It is worth noting that in the mm and THz ranges, the behavior of metals (e.g., Au, Ag, Cu) is close to the one of a PEC. From the fabrication point of view, with the development of 3D printing technology specially with mm and m resolutions, such structures can be easily realized in the THz and GHz ranges. The growing number of materials that are compatible with additive manufacturing provides many degrees of freedom for the fabrication [68]. Moreover, in the nm and  $\mu\text{m}$  length scales,  $e$ -beam lithography [69], with the assistance of ion milling, dry and wet etching, and deposition techniques, can be used [70,71]. Laser writing [72] is also an alternative.

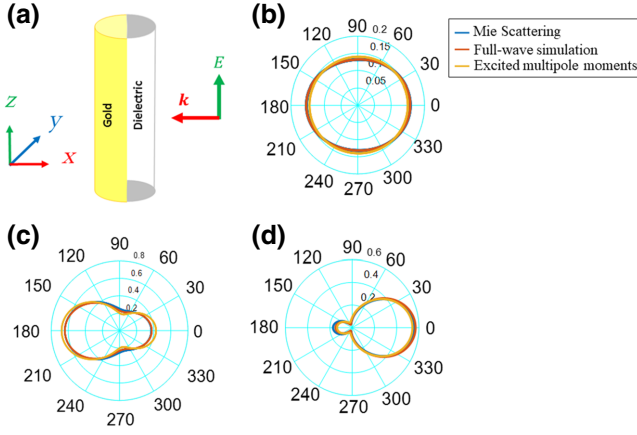


FIG. 2. (a) Schematic showing a metal-dielectric metacylinder ( $\epsilon_r = 18$ ) with a wedge angle of  $\pi$ , which is excited by TM-polarized waves propagating on the  $-x$  direction. Far-field scattering pattern from a mentioned meta-atom with different radius (b) 600 nm, (c) 800 nm, and (d)  $1 \mu\text{m}$  using Mie scattering, full-wave simulation, and excited multipole moments.

It is clear from Fig. 2 that the radiation of the derived polarization is in good agreement with the full-wave simulation. It is noteworthy that the small difference between the scattering patterns is due to the truncation of the scattering series and the dipole approximation.

### B. Extraction of polarizability tensor

Due to the asymmetry of the proposed meta-atom, in contrast to the symmetric cases of the sphere and the cylinder meta-atoms, extraction of the polarizability tensor is complicated. There are several methods to extract the polarizability tensor for a desired bianisotropic meta-atom [66,67,73,74]. In this paper, we use the standing-wave approach to derive the polarizability tensor as presented in recent studies [66,67]. We can simply write a standing wave as a superposition of two plane waves traveling in opposite directions (see Fig. 3). Using the extracted EM multiple moments from the previous section, the polarizability tensors excited by the standing wave can be derived using the superposition theorem. As is clear from Fig. 3, the magnetic fields are out of phase in the center of coordinates, therefore by adding or subtracting the two plane waves we can derive the pure electric and magnetic components of the polarizability tensors, respectively. As an example 12 polarizability tensor components can be derived using  $E_x = E_0 e^{\pm jky}$  and  $H_z = \pm H_0 e^{\pm jky}$  plane waves.

$$\alpha_{qx}^{ee} = \frac{P_q^{3\pi/2} + P_q^{\pi/2}}{2E_0}, \quad \alpha_{qx}^{me} = \frac{M_q^{3\pi/2} + M_q^{\pi/2}}{2E_0} \quad (13)$$

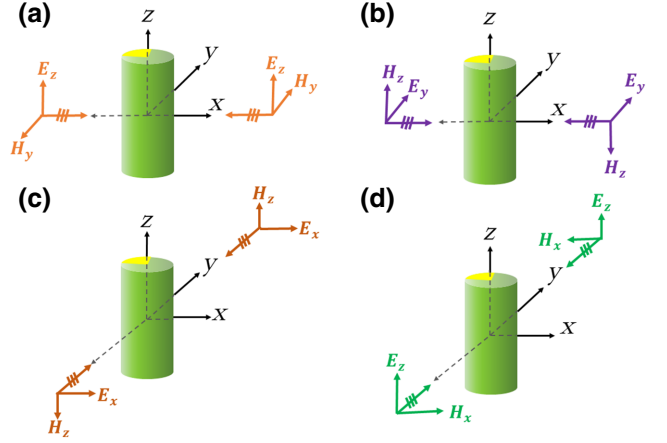


FIG. 3. Polarizability tensor extraction setup based on the standing-wave method introduced in Refs. [66,67]. In each setup, we can calculate the (a)  $\alpha_{zz}^{ee}, \alpha_{yz}^{me}, \alpha_{zy}^{em}, \alpha_{yy}^{mm}, \alpha_{xy}^{mm}$ ; (b)  $\alpha_{yy}^{ee}, \alpha_{xy}^{ee}, \alpha_{zy}^{me}, \alpha_{xz}^{em}, \alpha_{zz}^{em}, \alpha_{zz}^{mm}$ ; (c)  $\alpha_{xx}^{ee}, \alpha_{yx}^{ee}, \alpha_{yx}^{me}, \alpha_{zx}^{em}$ ; and (d)  $\alpha_{xz}^{me}, \alpha_{zx}^{em}, \alpha_{xx}^{mm}, \alpha_{yx}^{mm}$  individual polarizability components.

$$\alpha_{qz}^{em} = \frac{P_q^{3\pi/2} - P_q^{\pi/2}}{2E_0} Z_0, \quad \alpha_{qz}^{mm} = \frac{M_q^{3\pi/2} - M_q^{\pi/2}}{2E_0} Z_0, \quad (14)$$

where  $q = \{x, y, z\}$ , and moments superscripts (i.e.,  $\pi/2$  and  $3\pi/2$ ) indicate the wave-vector angle with respect to the direction  $x$ . All the other components can be derived by simply using different configurations for the standing wave (see Fig. 3) similar to Refs. [66,67]. After complete consideration of all the derived polarizability tensor components, the complete polarizability tensor can be presented as follows:

$$\begin{bmatrix} P \\ M \end{bmatrix} = \begin{bmatrix} \alpha_{xx}^{ee} & \alpha_{xy}^{ee} & 0 & 0 & 0 & \alpha_{xz}^{em} \\ \alpha_{yx}^{ee} & \alpha_{yy}^{ee} & 0 & 0 & 0 & \alpha_{yz}^{em} \\ 0 & 0 & \alpha_{zz}^{ee} & \alpha_{zx}^{em} & \alpha_{zy}^{em} & 0 \\ 0 & 0 & \alpha_{xz}^{me} & \alpha_{xx}^{mm} & \alpha_{xy}^{mm} & 0 \\ 0 & 0 & \alpha_{yz}^{me} & \alpha_{yx}^{mm} & \alpha_{yy}^{mm} & 0 \\ \alpha_{zx}^{me} & \alpha_{zy}^{me} & 0 & 0 & 0 & \alpha_{zz}^{mm} \end{bmatrix} \begin{bmatrix} E_{\text{loc}} \\ H_{\text{loc}} \end{bmatrix}. \quad (15)$$

One should note that an analytical and compact form of the polarizability tensor components is extracted and presented in Appendix C. We normalize all the presented polarizabilities to provide fair comparison:  $\alpha_{ee}, \alpha_{em}, \alpha_{me}$ , and  $\alpha_{mm}$  are normalized, respectively, to  $\epsilon_0, (\epsilon_0 Z_0)^{-1}, Z_0$ , and 1.

It is self-evident from the above relations that the induced polarizability tensor components depend on the Mie coefficients (wedge angle and dielectric constitutive parameters) and the meta-atom orientation, which make this meta-atom an excellent candidate for engineering and tuning of its EM response. The present analysis has

allowed us to define a fully dynamic expression for the entire polarizability tensor of the metal-dielectric metacylinder in closed form. In the following section, we discuss the properties of this tensor and present some practical examples.

#### IV. PROPERTIES OF THE POLARIZABILITY TENSOR

The polarizability tensor extracted in the previous section provides a fully dynamic, compact description of the EM response of a metal-dielectric metacylinder excited by an arbitrary electromagnetic wave. As noted, the validity of the tensor is limited to the case where the meta-atom is smaller than the wavelength. Also, its scattering response can be approximated by using only the electric and magnetic dipole terms. Although our derivation considered an infinitely long metal-dielectric metacylinder, the Mie-scattering results are well known to characterize a finite meta-atom with a length to diameter ratio of greater than 5 [32].

We verify our results by simply comparing the polarizability components for the special case of an infinitely long dielectric cylinder ( $\beta = 0$ ) in both static [32] and dynamic regimes [33]. The static polarizability components for dielectric cylinder are  $\alpha_{zz}^{ee} = \pi r_0^2 (\epsilon_r - 1)$  and  $\alpha_{xx}^{mm} = \alpha_{yy}^{mm} = 0$ ; we normalize the polarizability components to the cross section for an easier comparison with the static polarizability components for an electrically long cylinder. Figure 4 shows that the normalized transverse magnetic [ $\alpha_{xx,yy}^{mm} / (\pi r_0^2)$ ] and longitudinal electric polarizabilities [ $\alpha_{zz}^{ee} / (\pi r_0^2)$ ] are in good agreement with results of Refs. [32,33].

The overarching objective of developing a tunable meta-atom is to enable the design of any desired EM response, that is, to engineer a meta-atom for any given polarizability tensor. To date, there are only a handful of meta-atoms represented by a closed-form EM response [33,75]. Further, it is noteworthy that the EM response of these meta-atoms

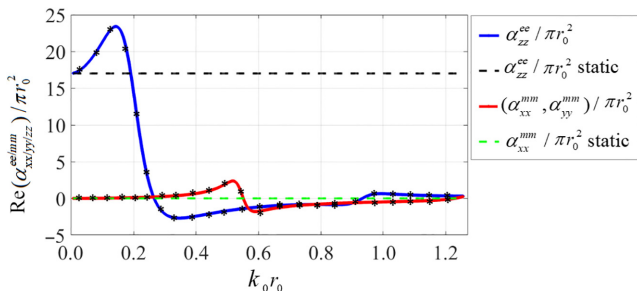


FIG. 4. Static and dynamic transverse magnetic polarizability, and longitudinal electric polarizability of a dielectric cylinder ( $\epsilon_r = 18$ ) excited by a TM-polarized incident wave. We vary here the electrical size  $k_0 r_0$ . The star-shaped markers represent a validation based on Refs. [32,33]. The plot shows the real parts of the polarizability components.

is limited owing to the simplicity and symmetry of their structures. However, the metal-dielectric metacylinder presented here is capable of realizing complex EM responses through the tunability of its polarizability tensor. The geometry of the presented meta-atom clearly shows that we have several degrees of freedom. We can simply tune the EM response and polarizability tensor by changing the constitutive and geometric parameters such as dielectric properties, wedge angle, and angle of rotation. These parameters affect the resonant frequency and the strength of the induced magnetic, electric, and magnetoelectric responses.

Since the tunability of the dielectric permittivity is limited to existing materials, the wedge angle plays an important role in the design of the meta-atom. Figures 5 and 6 illustrate the effect of wedge angle on the strength and position of the resonance with respect to the metacylinder radius. Here, we choose to illustrate a set of selected polarizability components for conciseness. Examining Figs. 5 and 6, we see that the resonant frequency of the polarizability components excited by the TM wave can be tuned by adjusting the  $\beta$  angle. However, adjusting the wedge angle affects only the strength of the resonance in the TE excitation. This result is due to the use of a nonmagnetic dielectric in the meta-atom. Nevertheless, it is possible to simultaneously adjust both the strength and position of resonance with wedge angle when using a magnetic dielectric in the meta-atom. The presence of magnetoelectric effects in such a simple structure might be surprising at first sight. In fact, the geometrical asymmetry and inhomogeneity of this meta-atom breaks the symmetry in EM response and allows for the magnetoelectric effects to arise. One can also deduce this result from the standing-wave approach. The EM response of an asymmetric structure is dissimilar for incident waves with opposite propagation directions, that is, the superposition of induced magnetic dipoles [see Eqs. (11) and (12)] give rise to magnetoelectric polarizability components.

#### V. ILLUSTRATIVE APPLICATIONS

By controlling the proposed nanostructure's Mie resonance modes, we can attain a large number of nontrivial effects. Design of asymmetrical meta-atoms avail numerous applications in photonics. Breaking the geometrical symmetry leads to a high degree of freedom for engineering unconventional EM responses. In the following, we prove that the proposed meta-atom breaks azimuthal symmetry by reducing the coefficient associated with  $\sin(n\phi)$  modes to zero [61]. Based on our notation this condition leads to the following equation for electric dipole modes under TE illumination:

$$\left| \left( a_1^{\text{TE}} - j b_1^{\text{TE}} \right) \cos(\alpha) + \left( b_1^{\text{TE}} + j a_1^{\text{TE}} \right) \sin(\alpha) \right| \neq 0 \quad (16)$$

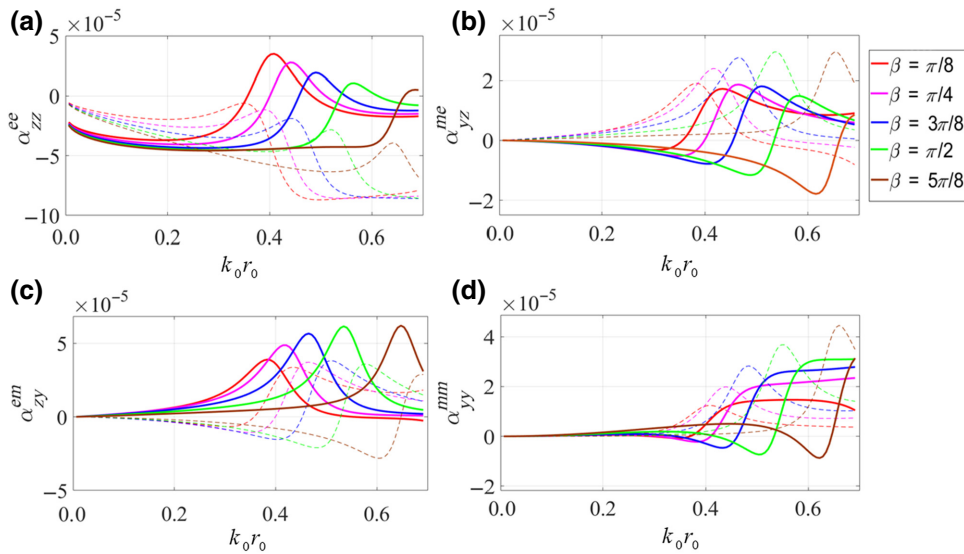


FIG. 5. Real (solid lines) and imaginary parts (dashed lines) of (a) electric, (b),(c) magneto-electric, and (d) magnetic normalized dipole polarizability of the asymmetric metal-dielectric metacylinder ( $\epsilon_r = 18$ ), which is excited by the TM-polarized incident wave for variant values of  $\beta$  with respect to radius.

$$\left| \left( a_1^{\text{TE}} + j b_1^{\text{TE}} \right) \cos(\alpha) + \left( b_1^{\text{TE}} - j a_1^{\text{TE}} \right) \sin(\alpha) \right|.$$

The inequality in the above equation, which can be tuned by changing  $\alpha$ , is clearly the result of breaking the azimuthal symmetry in the system. This condition can lead to an unbalanced power radiation. Therefore, the proposed meta-atom can be designed (by adjusting  $\alpha$ ) to achieve a desired unbalanced scattering pattern for beam deflection applications.

In fact, breaking the azimuthal symmetry and attaining normal polarizability components are essential for design of meta-atomic structures used for various applications [49,50,61].

Hereunder, we divide the applications of the proposed metacylinder to two different categories.

(1) *The microscopic level applications:* engineering the EM wave scattering of a single meta-atom, in which a dipole free response is desired.

(2) *The macroscopic level application:* design of a metasurface processor consisting of densely packed metacylinders for optical signal processing and image processing (i.e., edge detection).

### A. Meta-atom: near-zero scattering

First, we look for a condition where the electric polarization  $\mathbf{P}$  in the meta-atom can be made negligible (electric dipole-free meta-atom). We assume that the meta-atom is illuminated by a TM-polarized plane wave propagating in the  $x$  direction. According to Eq. (11) the electric polarization  $P_z$  directly depends on the first harmonic of Mie scattering ( $a_0$ ) of the metal-dielectric metacylinder. Targeting  $a_0 = 0$  as a goal of the optimization, we obtain

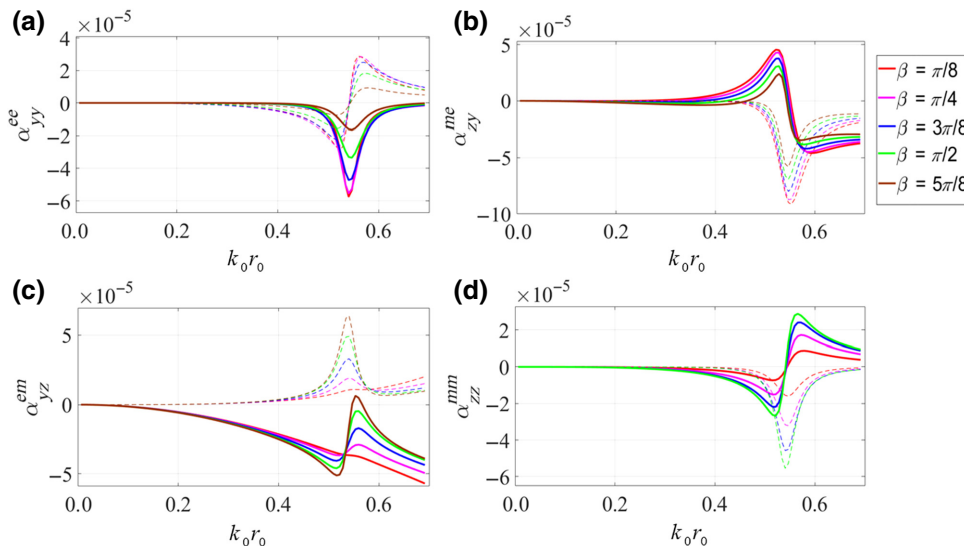


FIG. 6. Real (solid lines) and imaginary parts (dashed lines) of (a) electric, (b),(c) magneto-electric, and (d) magnetic normalized dipole polarizability of the asymmetric metal-dielectric metacylinder ( $\epsilon_r = 18$ ), which is excited by the TE-polarized incident wave for variant values of  $\beta$  with respect to radius.

the conditions under which the induced electric dipole is nearly zero ( $\epsilon_r = 11.16, r_0 = 0.09\lambda_0, \alpha = 62.96^\circ, \beta = 125.27^\circ$ ). Figure 7(a) shows the magnitude of electric polarization  $P_z$  and transverse magnetic polarization  $M_t$ . Under this condition electric quadrupoles and magnetic dipoles entirely determine the wave-matter interaction, which is illustrated through the 3D scattering pattern of the optimized meta-atom. It is worth noting that it is not possible to achieve a precisely zero value for the electric dipole in a passive structure. However, a recent study shows that this condition can be achieved when using a meta-atom structure, which on the whole is lossless, that is, a structure comprising a loss-compensated dimer [76].

Another appealing application is to determine the condition under which forward and backward scattering of the meta-atom vanishes. Based on the optical theorem [77] the total extinction cross section of an object  $\sigma_{\text{ext}}$  (sum of absorption and total scattering cross sections) is related to the normalized scattering amplitude in the forward direction  $\sigma_\varphi(0)$  in the following way:

$$\sigma_{\text{ext}} = \frac{\lambda_0^2}{\pi} \text{Im}[\sigma_\varphi(0)], \quad (17)$$

where  $\lambda_0$  is the operating wavelength. Optical theorem applies to the EM response of any object illuminated by a linearly polarized plane wave. Equation (17) implies that a near-zero forward scattering amplitude results in zero total scattering, which means that a meta-atom with near-zero forward scattering will be transparent. Recent studies have demonstrated that in order for forward scattering to be zero, part of the meta-atom must be active. Therefore, in the passive case it is not possible to achieve exactly zero forward scattering [76,77]. Assuming that the meta-atom does not consist of absorptive material, the extinction cross section and scattering cross section would be equal. Hence, the total cross section can be calculated using the scattering

fields in the following way:

$$\sigma_T = \frac{1}{2\pi} \int_0^{2\pi} \sigma(\varphi) d\varphi \quad (18)$$

$$\frac{\sigma_T}{4r_0} = \frac{1}{2k_0 r_0} \left\{ \sum_{n=0}^{\infty} |a_n^{\text{sca}}|^2 \epsilon_n + \sum_{n=1}^{\infty} |b_n^{\text{sca}}|^2 \right\}. \quad (19)$$

Now that we have the analytical expression for EM scattering from the proposed meta-atom, we can easily find the condition under which the forward and backward scattering are near-zero and zero, respectively. Figures 7(b) and 7(c) present the near-zero or zero forward and backward scattering pattern under these specific conditions.

Here, the specific properties of the structure, which possess near-zero or zero forward and backward scattering are presented. The electrical permittivity of the dielectric, radius of the cylinder, rotation angle, and wedge angle of a meta-atom with near-zero forward scattering are as follows: ( $\epsilon_r = 17.5, r_0 = 0.0507\lambda_0, \alpha = 90.01^\circ, \beta = 0.1^\circ$ ). In this case one can approximate the metal part of the wedge with a simple thin metallic sheet, which possesses the same response. While the fabrication of sharp edges in the telecommunication range (i.e.,  $r > 1 \mu\text{m}$ ) is feasible with the help of *e*-beam lithography [78], and additive manufacturing can be employed at lower frequencies [79], some geometrical imperfections are expected, which may result in frequency shifts that may slightly alter the overall polarization properties of the meta-atom. Figure 7(b) illustrates the 2D scattering of the meta-atom with the aforementioned properties and the total scattering with respect to wavelength. A similar condition for zero backscattering is found ( $\epsilon_r = 14.807, r_0 = 0.0721\lambda_0, \alpha = 279.87^\circ, \beta = 51.36^\circ$ ) and the corresponding scattering pattern is shown in Fig. 7(b). Figure 7(b) shows that the forward scattering and the total cross section are highly correlated and that the minimum total scattering and the forward scattering occur at the same wavelength.

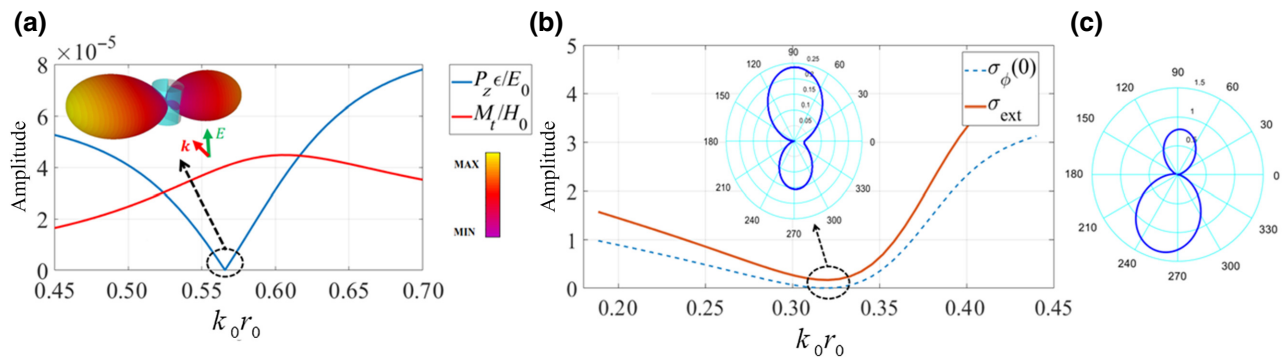


FIG. 7. (a) Magnitude of electric polarization  $P_z$  and transverse magnetic polarization  $M_t$  with respect to radius and 3D scattering pattern for optimized electric dipole-free meta-atom. (b) Total extinction cross section ( $\sigma_{\text{ext}}$ ) and forward scattering [ $\sigma_\varphi(0)$ ] with respect to radius and polar scattering pattern of the optimized meta-atom for near-zero forward scattering and (c) backward scattering.



### B. Metasurface processor: advanced spatial optical signal processing

With the existing digital processing and integrated circuit technologies reaching physical limitation of Moore's law (number of transistors per area unit), recently, the interest in analog computing was revived with the introduction of wave-based spatial metasurface processors, due to various advantages such as compact single-block architecture, high-speed response, and low-energy consumption compared to the conventional electronic-based devices [47,54,55]. As a result, to overcome some of the speed restrictions and power-consumption drawbacks of existing digital signal processors, the proposed material-based optical computing devices could potentially replace all or some of the digital processing building blocks, exploiting photons instead of electron-hole pairs to carry out the desired processing operations. However, the problem of implementing optical analog memories to capture and store the results remains an open challenge to date. For example, the remaining detection blocks in the proposed computing designs still must consist of digital components. One of the main challenges of optical signal processing today, is to design an optical spatial filter with an asymmetrical (i.e., odd) OTF response capable of distinguishing between  $-k_t$  and  $k_t$  propagation at normal incidence. The asymmetrical OTF response is required for first-order differentiation using metasurface processors [47,49–51,53,55,80]. Herein, we discuss the ability of the proposed meta-atom to engineer asymmetrical OTF responses by virtue of tuning the wedge angle and the dielectric constant making this structure amenable to processing applications such as first-order differentiation. Consider a homogeneous passive reciprocal metasurface layer comprising the proposed metacylinders located at the  $y = 0$  plane, where  $\psi_{\text{inc}}(x)$  and  $\psi_{\text{ref/trans}}(x)$  are the input and output signals of this linear optical system [see Fig. 8(a)]. The angular EM response

of the metasurface processor determines its corresponding OTF response in the spatial Fourier domain [i.e.,  $\tilde{H}(k_x)$ ]. The output signal  $\psi_{\text{inc}}(x)$  can be calculated given the input signal  $\psi_{\text{ref/trans}}(x)$  using  $\psi_{\text{ref/trans}}(x) = F^{-1}\{\tilde{H}(k_x) \times F[\psi_{\text{inc}}(x)]\}$ , where  $k_x$  denotes the spatial frequency variable in the Fourier space,  $F$  and  $F^{-1}$  represent the Fourier and inverse Fourier transforms, respectively. Here, we first analyze a metasurface processor, that is an array of electric and magnetic dipoles comprising both tangential ( $t$  subscript) and normal ( $n$  subscript) components.

The spatial transfer function associated with the metasurface processor can be modeled using the vectorial form of the generalized sheet boundary conditions [82].

$$\mathbf{E}_t^+ \times \hat{\mathbf{n}} - \mathbf{E}_t^- \times \hat{\mathbf{n}} = -j\omega \left( \mathbf{M}_t - \hat{\mathbf{n}} \times \frac{\mathbf{k}_t}{\omega\epsilon} P_n \right), \quad (20)$$

$$\hat{\mathbf{n}} \times \mathbf{H}_t^+ - \hat{\mathbf{n}} \times \mathbf{H}_t^- = -j\omega \left( \mathbf{P}_t + \hat{\mathbf{n}} \times \frac{\mathbf{k}_t}{\omega\mu} M_n \right), \quad (21)$$

where  $\epsilon$  and  $\mu$  are the permittivity and permeability of the surrounding medium, respectively.  $\hat{\mathbf{n}}$  is the unity vector normal to the metasurface plane (i.e.,  $\hat{\mathbf{y}}$ ). The  $+$  and  $-$  superscripts refer to the field values at  $y = 0^+$  and  $0^-$ , respectively. Moreover,  $t$  and  $n$  subscripts represent the tangential and normal components. In order to simplify Eqs. (20) and (21) we can introduce the equivalent magnetic and electric surface polarization densities in the following way:

$$\begin{aligned} \mathbf{M}_{t,\text{eq}} &= \mathbf{M}_t - \hat{\mathbf{n}} \times \frac{\mathbf{k}_t}{\omega\epsilon} P_n, \\ \mathbf{P}_{t,\text{eq}} &= \mathbf{P}_t + \hat{\mathbf{n}} \times \frac{\mathbf{k}_t}{\omega\mu} M_n. \end{aligned} \quad (22)$$

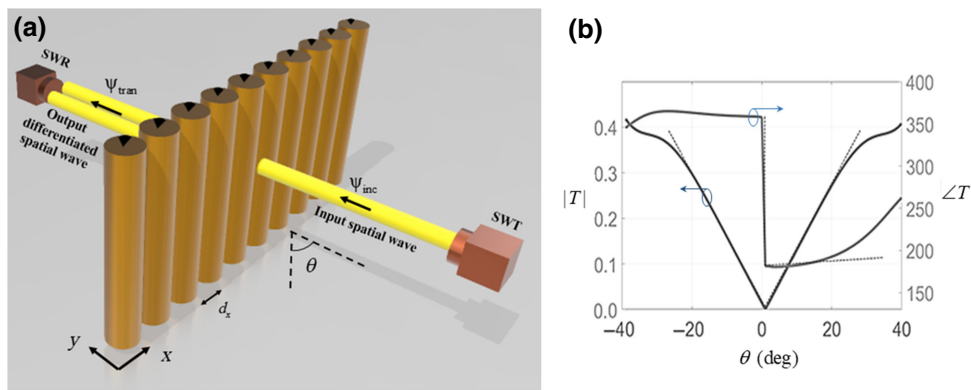


FIG. 8. (a) Array of metal-dielectric metacylinders (include silicon and gold [81] materials) as the metasurface processor. SWT and SWR are spatial wave transmitter and receiver, respectively. (b) Solid line: the amplitude and phase of synthesized OTF. Dashed line: the ideal OTF for the first-order differentiation operation. Simulation parameters:  $\lambda_0 = 4.16 \mu\text{m}$ ,  $r_0 = 0.9 \mu\text{m}$ ,  $\beta = 60^\circ$ ,  $\alpha = 150^\circ$ , and  $d_x = 2.5 \mu\text{m}$ .

Furthermore, the tangential components of the reflected  $E_r^i$  and transmitted  $E_t^i$  electric fields at the boundary of the metasurface are obtained

$$\mathbf{E}_r^i = \frac{j\omega\bar{\bar{Q}}}{2} \cdot \left[ \mathbf{P}_{t,\text{eq}} \mp \mathcal{Q}^{-1} \cdot \hat{\mathbf{n}} \times \mathbf{M}_{t,\text{eq}} \right], \quad (23)$$

$$\mathbf{E}_t^i = \mathbf{E}_t^i + \frac{j\omega\bar{\bar{Q}}}{2} \cdot \left[ \mathbf{P}_{t,\text{eq}} \pm \mathcal{Q}^{-1} \cdot \hat{\mathbf{n}} \times \mathbf{M}_{t,\text{eq}} \right]. \quad (24)$$

The derivation of  $\mathcal{Q}$ ,  $P_r$ , and  $P_n$  is outlined in Appendix D. To further simplify the equations  $\mathbf{M}_r = \mathbf{M}_n = 0$  can be considered for nonmagnetic materials. Thereafter, reflection and transmission coefficients are derived

$$R = \frac{j\omega Z_0}{2S} \left[ \hat{\alpha}_{xx}^{ee} |\cos \theta| - \frac{\hat{\alpha}_{yy}^{ee} \sin^2 \theta}{|\cos \theta|} \right], \quad (25)$$

$$T = \frac{j\omega Z_0}{2S} \left[ \hat{\alpha}_{xx}^{ee} |\cos \theta| \pm 2\hat{\alpha}_{xy}^{ee} \sin \theta + \frac{\hat{\alpha}_{yy}^{ee} \sin^2 \theta}{|\cos \theta|} \right], \quad (26)$$

where  $\hat{\alpha}^{ee}$  is the effective polarizability. Upon closer observation of Eq. (27), it is clear that an odd spatial OTF response [i.e.,  $\sin(\theta)$  angular variation] can only be achieved by exciting the  $\hat{\alpha}_{xy}^{ee}$  component on the metasurface processor. As we mention earlier in this section, achieving an odd OTF response is required for first-order differentiation, which highlights the ability of the proposed meta-atom to introduce normal polarizability components to the metasurface processor. Although the analytical formula describing the individual polarizability of the metacylinder is presented here, for the sake of brevity we avoid the mathematical derivation of effective polarizability tensor from individual polarizability components. The explicit analytical formula for the effective polarizability tensor from the individual polarizability tensor for a

dielectric cylinder is derived in Ref. [10,83]. For an array of cylinders and generally 2D meta-atoms, an analytical formula for effective polarizability components can be directly obtained from Ref. [10] by considering the coupling between the meta-atoms. Once again, our goal in this section is elaborating the necessary condition to achieve odd OTF response [i.e.,  $\sin(\theta)$  angular variation] based on the relation of transmission and reflection coefficients regarding the effective polarizability components.

Given the fact that the excitation of  $xy$  component of the effective polarizability necessitates the excitation of the respective component of the individual polarizability tensor, excitation of  $xy$  component in the individual polarizability is required for breaking the angular symmetry of transmission response (i.e., distinguishing between  $k_x$  and  $-k_x$ ). In Sec. III, we explicitly show that the proposed meta-atom is well capable of engineering  $xy$  polarizability component:

$$\alpha_{xy}^{ee} = -\frac{2 \left[ \Psi_{b,1}^{\text{TE},+} \cos(\alpha) - \Psi_{a,1}^{\text{TE},+} \sin(\alpha) \right]}{jk_0^2}, \quad (27)$$

where the value of  $\alpha_{xy}^{ee}$  can be engineered by virtue of tuning the geometrical properties of the meta-atom (i.e.,  $\beta$  and  $\alpha$ ).

Now that the  $xy$  polarizability can be achieved using the proposed metacylinder, we optimize the optical response of the metasurface processor comprising an array of metacylinders to achieve the metasurface differentiator's OTF response, that is  $H(k_x) = cjk_x = cjk \sin \theta$ , where  $c$  is a constant. This first-order differentiation operator is highly relevant for various applications in signal and image processing such as edge detection. Comparing the mentioned OTF response with Eq. (26) the optimization goal for the

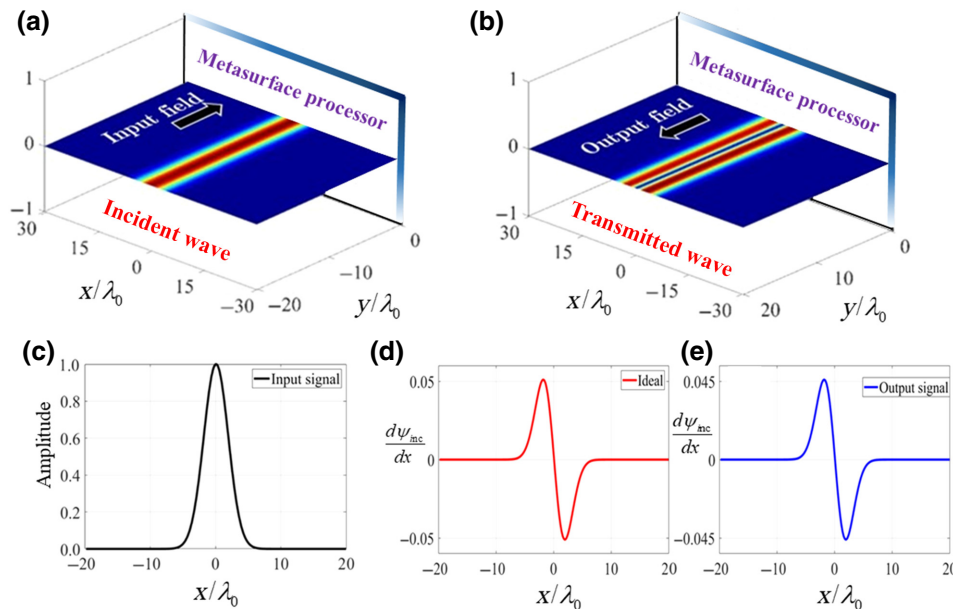


FIG. 9. (a),(c) Gaussian-shape incident-field profile with (b),(e) the transmitted derivative-field profile. (d) The exact derivative signals are also presented for the sake of comparison.

desired metasurface processor is derived:  $\alpha_{xx}^{ee} = \alpha_{yy}^{ee} = 0$  and for  $-30^\circ < \theta < 30^\circ$ .

Here, the geometry of the proposed meta-atom gives us the ability us to achieve this goal and synthesize the desired OTF response, which enables real-time first-order derivation (see Fig. 8). The proposed meta-atom can elaborately mimic the required  $k_x$ -dependency first-order differentiator [see Fig. 8(b)]. An excellent agreement between the transmission coefficient of the designed metasurface and the desired OTF response for both phase and amplitude is achieved for input signals with the normalized spectral beam width  $|W/k_0| < 0.3$ .

To verify the validity of the proposed metasurface differentiator performance of the employed metasurface processor, a Gaussian signal is considered as the input signals [see Figs. 9(a) and 9(b)]. The transmitted signal and the corresponding results are illustrated in Figs. 9(c)–9(e). To evaluate the performance of our metasurface differentiator, the numerically obtained result is compared with the first derivative of the input signal [see Fig. 9(d)]. An excellent agreement between output and first derivative is achieved.

As mentioned earlier, optical metasurface operators are highly advantageous in image processing. Here, in particular, the designed differentiator can be used for edge detection, which plays a momentous role in the image segmentation and the other image preprocessing steps [49,50]. To elaborate even further, object recognition with the help of spatial differentiation enables us to extract the

boundaries between two regions of different intensities. The proposed structure is capable of detecting edges and performing line-by-line differentiation with respect to the  $x$  axis for 2D images similar to Ref. [51]. To show the superior ability of the designed metasurface processor, a complex signal including Gaussian and sinusoidal functions is used for spatial signal processing [see Figs. 10(a) and 10(b)]. The transmitted signals are numerically simulated and the corresponding transverse-field profiles are displayed on Figs. 10(a) and 10(c). As expected, the 1D edge-detector metasurface successfully exposes all outlines of the normally incident image along the vertical orientations, exhibiting its higher sensibility to fine details as a first-order derivative operator.

## VI. CONCLUSION

An ideal meta-atom is one which contains all possible bianisotropic electromagnetic responses wherein the structure of the meta-atom permits independent tunability of all the elements comprising the constitutive parameters. Nevertheless, there will be some physical constraints to the design of any meta-atom. In this paper, we propose a metal-dielectric metacylinder as a tunable meta-atom, which consists of metallic and dielectric finite wedges. Numerous design parameters provide a good degree of freedom, which enable the proposed meta-atom to be an excellent candidate for engineering the EM response. We first derive the analytical expression for the EM scattering due to the structure. Next, we extract the polarizability tensor and explain the response of such a meta-atom in the dipole region. Finally, we show the flexibility of the proposed inclusion through practical applications in both microscopic and macroscopic levels. The examples verify the validity of the analytical formulation and illustrate the capability of the proposed meta-atom to independently tune the electromagnetic polarizability components.

## APPENDIX A: BOUNDARY CONDITIONS

In this appendix, we detail the analytical steps for deriving EM scattering from an asymmetric metal-dielectric metacylinder of infinite extent along its axis.

In the dielectric region, we construct an expansion for the total electric field  $E^d = E_z^d \hat{z}$  of the TM case, which follows from the solution of Maxwell's equations in cylindrical coordinates

$$E_z^d(r, \phi) = \sum_{i=0}^{\infty} \left\{ \zeta_{vi}^I J_{vi}(k_c r) \cos[vi(\phi + \alpha)] \right\} + \sum_{i=1}^{\infty} \left\{ \zeta_{\tau i}^{II} J_{\tau i}(k_c r) \sin[\tau i(\phi + \alpha)] \right\}, \quad (\text{A1})$$

where  $k_c = \omega \sqrt{\epsilon_c \mu_c}$  denotes the wave number. The  $\zeta^I$  and the  $\zeta^{II}$  are the (unknown) coefficients. Also, the incident

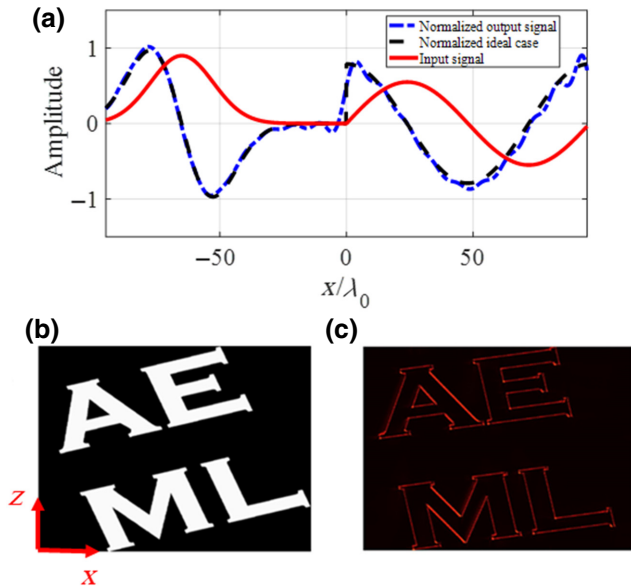


FIG. 10. Spatial signal processing by exploiting the proposed metasurface processor. (a) Complex input signal and normalized output and ideal case. (b) Input images and (c) edge-detected images when metasurface differentiator differentiates the input image along  $x$  direction. For the 2D image, differentiation is performed line by line along the  $x$  axis.

plane wave has the following form:

$$E_z^{\text{inc}}(r, \phi) = \sum_{n=0}^{\infty} \left\{ U_n^I J_n(k_0 r) \cos[n(\varphi + \alpha)] \right\} + \sum_{i=1}^{\infty} \left\{ U_n^{\text{II}} J_{\tau_i}(k_0 r) \sin[n(\varphi + \alpha)] \right\}, \quad (\text{A2})$$

where

$$U_n^I = \frac{2E_0 j^n}{\epsilon_n} \cos[n(\gamma + \alpha)], \quad (\text{A3})$$

$$U_n^{\text{II}} = 2E_0 j^n \sin[n(\gamma + \alpha)], \quad (\text{A4})$$

and also  $E_z^{\text{sc}}$  is presented in Eq. (1). On the metal part of the dielectric-metal metacylinder ( $r = r_0$ ) the tangential part of the total electric field must vanish, and at the dielectric-air interface ( $r = r_0$ ), the tangential parts of the total electric and total magnetic field have to be continuous.

$$E_z^{\text{sc}}|_{r=r_0} + E_z^{\text{inc}}|_{r=r_0} = \begin{cases} E_z^d|_{r=r_0} & S_1 < \phi < S_2 \\ 0 & \text{otherwise,} \end{cases} \quad (\text{A5})$$

$$H_\phi^{\text{sc}}|_{r=r_0} + H_\phi^{\text{inc}}|_{r=r_0} = H_\phi^d|_{r=r_0} \quad S_1 < \phi < S_2, \quad (\text{A6})$$

where  $S_1$  and  $S_2$  are  $-\pi + (\beta/2 + \alpha)$  and  $\pi - (\beta/2 + \alpha)$ .

Using the orthogonality relations of the trigonometric functions, we can compute the unknown scattering

coefficient ( $a_n$  and  $b_n$ ) in Eqs. (1) and (2), which are presented in Eqs. (5) and (6).

Also,  $\tau_i$ ,  $\nu_i$ ,  $\epsilon_n$ , and  $\delta_{nm}$  are defined in the following way:

$$\tau_i = \frac{i\pi}{\pi - \beta/2} \quad i = 1, 2, 3, \dots, \quad (\text{A7})$$

$$\nu_i = \frac{\pi(2i+1)}{2(\pi - \beta/2)} \quad i = 0, 1, 2, \dots, \quad (\text{A8})$$

$$\epsilon_n = \begin{cases} 2 & n = 0 \\ 1 & n \neq 0 \end{cases}, \quad (\text{A9})$$

$$\delta_{nm} = \begin{cases} 1 & n = m \\ 0 & n \neq m \end{cases}. \quad (\text{A10})$$

## APPENDIX B: SCATTERING COEFFICIENTS

The scattering coefficients of metal-dielectric meta-atom  $a_n$  and  $b_n$  are derived using the EM boundary conditions. Further, these can be written in the following way where “e” and “o” superscripts allude to the even and odd modes in the Mie-scattering coefficient.

$$[a_n^{\text{TM/TE}}]_{n \times 1} = [\tau_n]_{1 \times n} [\chi_{nm}^{(e), \text{TM/TE}}]_{n \times m}^{-1} [\Upsilon_m^{(e), \text{TM/TE}}]_{m \times 1}, \quad (\text{B1})$$

$$[b_n^{\text{TM/TE}}]_{n \times 1} = [\tau_n]_{1 \times n} [\chi_{nm}^{(o), \text{TM/TE}}]_{n \times m}^{-1} [\Upsilon_m^{(o), \text{TM/TE}}]_{m \times 1}, \quad (\text{B2})$$

where the  $\chi_{nm}^{(e), \text{TM}}$ ,  $\tau_n$ , and  $\Upsilon_m^{(e), \text{TM}}$  are given by

$$\tau_n = \frac{1}{\left. \frac{dH_n^1(k_0 r)}{dk_0 r} \right|_{r=r_0}}, \quad (\text{B3})$$

$$\chi_{nm}^{(e)} = \frac{H_n^1(k_0 r_0)}{\left. \frac{dH_n^1(k_0 r)}{dk_0 r} \right|_{r=r_0}} \pi \epsilon_n \delta_{nm} - \sum_{i=0}^{\infty} \frac{Z_c(\pi - \beta/2)}{Z_0} \frac{J_{\nu_i}(k_c r_0)}{\left. \frac{dJ_{\nu_i}(k_c r)}{dk_c r} \right|_{r=r_0}} \times \left\{ \text{sinc} \left[ \frac{(\pi - \beta/2)(\nu_i - n)}{\pi} \right] + \text{sinc} \left[ \frac{(\pi - \beta/2)(\nu_i + n)}{\pi} \right] \right\} \times \left\{ \text{sinc} \left[ \frac{(\pi - \beta/2)(\nu_i - m)}{\pi} \right] + \text{sinc} \left[ \frac{(\pi - \beta/2)(\nu_i + m)}{\pi} \right] \right\}, \quad (\text{B4})$$

$$\Upsilon_m^{(e)} = -a_m^{\text{inc}} J_m(k_0 r_0) \pi \epsilon_m + \sum_{i=0}^{\infty} \frac{Z_c(\pi - \beta/2)}{Z_0} \frac{J_{\nu_i}(k_c r_0)}{\left. \frac{dJ_{\nu_i}(k_c r)}{dk_c r} \right|_{r=r_0}} \times \left\{ \text{sinc} \left[ \frac{(\pi - \beta/2)(\nu_i - m)}{\pi} \right] + \text{sinc} \left[ \frac{(\pi - \beta/2)(\nu_i + m)}{\pi} \right] \right\} \times \sum_{n=0}^{\infty} a_n^{\text{inc}} \left. \frac{dJ_n(k_0 r)}{dk_0 r} \right|_{r=r_0} \left\{ \text{sinc} \left[ \frac{(\pi - \beta/2)(\nu_i - n)}{\pi} \right] + \text{sinc} \left[ \frac{(\pi - \beta/2)(\nu_i + n)}{\pi} \right] \right\}. \quad (\text{B5})$$

Polarizability tensor components		
$\alpha_{zz}^{ee} = \frac{2\Psi_{a,0}^{\text{TM},+}}{jk_0^2}$	$\alpha_{yz}^{me} = -\frac{\Psi_{a,1}^{\text{TM},+} \cos(\alpha) + \Psi_{b,1}^{\text{TM},+} \sin(\alpha)}{jk_0^2}$	$\alpha_{zy}^{em} = \frac{2\Psi_{a,0}^{\text{TM},-}}{jk_0^2}$
$\alpha_{yy}^{mm} = -\frac{[\Psi_{a,1}^{\text{TM},-} \cos(\alpha) + \Psi_{b,1}^{\text{TM},-} \sin(\alpha)]}{jk_0^2}$	$\alpha_{xy}^{mm} = \frac{[\Psi_{b,1}^{\text{TM},-} \cos(\alpha) - \Psi_{a,1}^{\text{TM},-} \sin(\alpha)]}{jk_0^2}$	$\alpha_{yy}^{ee} = \frac{2[\Psi_{a,1}^{\text{TE},+} \cos(\alpha) + \Psi_{b,1}^{\text{TE},-} \sin(\alpha)]}{jk_0^2}$
$\alpha_{xy}^{ee} = -\frac{2[\Psi_{b,1}^{\text{TE},+} \cos(\alpha) - \Psi_{a,1}^{\text{TE},+} \sin(\alpha)]}{jk_0^2}$	$\alpha_{zy}^{me} = \frac{2\Psi_{a,0}^{\text{TE},+}}{jk_0^2}$	$\alpha_{zy}^{em} = \frac{2[\Psi_{a,1}^{\text{TE},-} \cos(\alpha) + \Psi_{b,1}^{\text{TE},-} \sin(\alpha)]}{jk_0^2}$
$\alpha_{xz}^{em} = -\frac{2[\Psi_{b,1}^{\text{TE},-} \cos(\alpha) - \Psi_{a,1}^{\text{TE},-} \sin(\alpha)]}{jk_0^2}$	$\alpha_{zz}^{mm} = \frac{2\Psi_{a,0}^{\text{TE},-}}{jk_0^2}$	$\alpha_{xx}^{ee} = -\frac{2[\Psi_{b,1}^{\text{TE},+} \cos(\alpha) - \Psi_{a,1}^{\text{TE},+} \sin(\alpha)]}{jk_0^2}$
$\alpha_{yx}^{ee} = \frac{2[\Psi_{a,1}^{\text{TE},+} \cos(\alpha) + \Psi_{b,1}^{\text{TE},+} \sin(\alpha)]}{jk_0^2}$	$\alpha_{zx}^{me} = \frac{2\Psi_{a,0}^{\text{TE},+}}{jk_0^2}$	$\alpha_{xz}^{me} = \frac{[\Psi_{b,1}^{\text{TM},+} \cos(\alpha) - \Psi_{a,1}^{\text{TM},+} \sin(\alpha)]}{jk_0^2}$
$\alpha_{zx}^{em} = \frac{2\Psi_{a,0}^{\text{TM},-}}{jk_0^2}$	$\alpha_{xx}^{mm} = \frac{[\Psi_{b,1}^{\text{TM},-} \cos(\alpha) - \Psi_{a,1}^{\text{TM},-} \sin(\alpha)]}{jk_0^2}$	$\alpha_{yx}^{mm} = -\frac{[\Psi_{a,1}^{\text{TM},-} \cos(\alpha) + \Psi_{b,1}^{\text{TM},-} \sin(\alpha)]}{jk_0^2}$

The relations for  $\chi_{nm}^{(o),\text{TM}}$  and  $\gamma_m^{(o),\text{TM}}$  can be written similar to  $\chi_{nm}^{(e),\text{TM}}$  and  $\gamma_m^{(e),\text{TM}}$  using the following substitutions:  $vi \rightarrow \tau i$ ,  $\varepsilon_n \rightarrow 1$ ,  $a_m^{\text{inc}} \rightarrow b_m^{\text{inc}}$ ,  $\text{sinc}(\theta_1) + \text{sinc}(\theta_2) \rightarrow \text{sinc}(\theta_1) - \text{sinc}(\theta_2)$ , and  $(i = n = 0) \rightarrow (i = n = 1)$  (indexes of the summation). Also the dual relations for  $\chi_{nm}^{(o),\text{TE}}$  and  $\gamma_m^{(o),\text{TE}}$  can be written with the following substitutions in  $\chi_{nm}^{(o),\text{TM}}$  and  $\gamma_m^{(o),\text{TM}}$ :  $vi \rightarrow \tau i$ ,  $\tau i \rightarrow vi$ ,  $J_n(\chi), H_n(\chi) \Rightarrow dJ_n(\chi)/d\chi, dH_n(\chi)/d\chi$  and  $Z_c(\pi - \beta/2)/Z_0 \rightarrow Z_c(\pi - \beta/2)/\varepsilon_i Z_0$ , where  $Z_0$  and  $Z_c$  are wave impedance of background medium and dielectric cylinder, respectively.

### APPENDIX C: POLARIZABILITY TENSOR COMPONENTS

In order to present a compact expression for the extracted polarizability tensor components, we define the following arbitrary parameters, which depend on the Mie coefficients:

$$\psi_{N,M}^{R,\pm} = N_M^{R,2\pi} \pm N_M^{R,\pi}, \quad (\text{C1})$$

$$\dagger \psi_{N,M}^{R,\pm} = N_M^{R,3\pi/2} \pm N_M^{R,\pi/2}, \quad (\text{C2})$$

where  $R = \text{TM}$  or  $\text{TE}$ ,  $N = a$  or  $b$  and  $M = 0$  or  $1$ .

Using the above expressions, the nonzero polarizability components are obtained as follows:

### APPENDIX D: EFFECTIVE ELECTRIC POLARIZATION ( $\mathbf{P}$ ) AND $2 \times 2$ DYADIC FUNCTION ( $\bar{\mathcal{Q}}$ )

$$\bar{\mathcal{Q}} = \eta \left( |\cos \theta| \frac{\mathbf{k}_t \mathbf{k}_t}{k_t^2} + \frac{1}{|\cos \theta|} \frac{\hat{\mathbf{n}} \times \mathbf{k}_t \hat{\mathbf{n}} \times \mathbf{k}_t}{k_t^2} \right), \quad (\text{D1})$$

$$\mathbf{P}_t = \left[ \hat{\alpha}_{xx}^{ee} \cos \theta + \hat{\alpha}_{xy}^{ee} \sin \theta \right] \frac{\mathbf{E}_t^i}{S}, \quad (\text{D2})$$

$$P_n = \left[ \hat{\alpha}_{yx}^{ee} \cos \theta + \hat{\alpha}_{yy}^{ee} \sin \theta \right] \frac{E_n^i}{S}. \quad (\text{D3})$$

- [1] Constantine A. Balanis, Antenna theory: A review, *Proc. IEEE* **80**, 7 (1992).
- [2] Walter Rotman, Plasma simulation by artificial dielectrics and parallel-plate media, *IRE Trans. Antennas Propagation* **10**, 82 (1962).
- [3] D. R. Smith and D. Schurig, Electromagnetic Wave Propagation in Media with Indefinite Permittivity and Permeability Tensors, *Phys. Rev. Lett.* **90**, 077405 (2003).
- [4] W. T. Lu and S. Sridhar, Superlens imaging theory for anisotropic nanostructured metamaterials with broadband all-angle negative refraction, *Phys. Rev. B* **77**, 233101 (2008).
- [5] Alexander Poddubny, Ivan Iorsh, Pavel Belov, and Yuri Kivshar, Hyperbolic metamaterials, *Nat. Photonics* **7**, 948 (2013).
- [6] Constantin Simovski, Stanislav Maslovski, Igor Nefedov, and Sergei Tretyakov, Optimization of radiative heat transfer in hyperbolic metamaterials for thermophotovoltaic applications, *Opt. Express* **21**, 14988 (2013).
- [7] Tiago A. Morgado, João S. Marcos, Mário G. Silveirinha, and Stanislav I. Maslovski, Ultraconfined Interlaced Plasmons, *Phys. Rev. Lett.* **107**, 063903 (2011).
- [8] John B. Pendry, A. J. Holden, W. J. Stewart, and I. Youngs, Extremely low Frequency Plasmons in Metallic Mesostructures, *Phys. Rev. Lett.* **76**, 4773 (1996).
- [9] Mário G. Silveirinha and Carlos A. Fernandes, Nonresonant structured material with extreme effective parameters, *Phys. Rev. B* **78**, 033108 (2008).
- [10] Marine Laroche, Silvia Albaladejo, Raquel Gómez-Medina, and Juan José Sáenz, Tuning the optical response of nanocylinder arrays: An analytical study, *Phys. Rev. B* **74**, 245422 (2006).

- [11] Petru Ghenuche, Grégory Vincent, Marine Laroche, Nathalie Bardou, Riad Haïdar, Jean-Luc Pelouard, and Stéphane Collin, Optical Extinction in a Single Layer of Nanorods, *Phys. Rev. Lett.* **109**, 143903 (2012).
- [12] Jeffrey M. McMahon, Stephen K. Gray, and George C. Schatz, Nonlocal Optical Response of Metal Nanostructures with Arbitrary Shape, *Phys. Rev. Lett.* **103**, 097403 (2009).
- [13] Pekka Ikonen, Constantin Simovski, and Sergei Tretyakov, Compact directive antennas with a wire-medium artificial lens, *Microw. Opt. Technol. Lett.* **43**, 467 (2004).
- [14] Filippo Capolino, *Theory and Phenomena of Metamaterials* (CRC Press, Boca Raton, Florida, 2017).
- [15] Mohammad Mahdi Salary and Hossein Mosallaei, Electrically tunable metamaterials based on multimaterial nanowires incorporating transparent conductive oxides, *Sci. Rep.* **7**, 10055 (2017).
- [16] Ali Momeni, Kasra Rouhi, Hamid Rajabalipanah, and Ali Abdolali, An information theory-inspired strategy for design of re-programmable encrypted graphene-based coding metasurfaces at terahertz frequencies, *Sci. Rep.* **8**, 6200 (2018).
- [17] Jianfa Zhang, Kevin F. MacDonald, and Nikolay I. Zheludev, Near-infrared trapped mode magnetic resonance in an all-dielectric metamaterial, *Opt. Express* **21**, 26721 (2013).
- [18] Anders Pors and Sergey I. Bozhevolnyi, Plasmonic metasurfaces for efficient phase control in reflection, *Opt. Express* **21**, 27438 (2013).
- [19] Junjie Du, Zhifang Lin, S. T. Chui, Guangjiong Dong, and Weiping Zhang, Nearly Total Omnidirectional Reflection by a Single Layer of Nanorods, *Phys. Rev. Lett.* **110**, 163902 (2013).
- [20] Ahmet Ali Yanik, Ronen Adato, Shyamsunder Erramilli, and Hatice Altug, Hybridized nanocavities as single-polarized plasmonic antennas, *Opt. Express* **17**, 20900 (2009).
- [21] Hamid Rajabalipanah, Ali Abdolali, Javad Shabanpour, Ali Momeni, and Ahmad Cheldavi, Asymmetric spatial power dividers using phase-amplitude metasurfaces driven by Huygens principle, *ACS Omega* **4**, 14340 (2019).
- [22] Mehdi Kiani, Majid Tayarani, Ali Momeni, Hamid Rajabalipanah, and Ali Abdolali, Self-biased tri-state power-multiplexed digital metasurface operating at microwave frequencies, *Opt. Express* **28**, 5410 (2020).
- [23] Mehdi Kiani, Ali Momeni, Majid Tayarani, and Can Ding, Spatial wave control using a self-biased nonlinear metasurface at microwave frequencies, *Opt. Express* **28**, 35128 (2020).
- [24] B. D. F. Casse, W. T. Lu, Y. J. Huang, E. Gultepe, L. Menon, and S. Sridhar, Super-resolution imaging using a three-dimensional metamaterials nanolens, *Appl. Phys. Lett.* **96**, 023114 (2010).
- [25] Gennady Shvets, S. Trendafilov, J. B. Pendry, and A. Sarychev, Guiding, Focusing, and Sensing on the Subwavelength Scale Using Metallic Wire Arrays, *Phys. Rev. Lett.* **99**, 053903 (2007).
- [26] Mário G. Silveirinha, Nonlocal homogenization model for a periodic array of  $\epsilon$ -negative rods, *Phys. Rev. E* **73**, 046612 (2006).
- [27] Stanislav I. Maslovski and Mário G. Silveirinha, Mimicking boyer's casimir repulsion with a nanowire material, *Phys. Rev. A* **83**, 022508 (2011).
- [28] Jie Yao, Xiaodong Yang, Xiaobo Yin, Guy Bartal, and Xiang Zhang, Three-dimensional nanometer-scale optical cavities of indefinite medium, *Proc. Natl. Acad. Sci.* **108**, 11327 (2011).
- [29] Zubin Jacob, Igor I. Smolyaninov, and Evgenii E. Narimanov, Broadband Purcell effect: Radiative decay engineering with metamaterials, *Appl. Phys. Lett.* **100**, 181105 (2012).
- [30] C. L. Cortes, W. Newman, S. Molesky, and Z. Jacob, Quantum nanophotonics using hyperbolic metamaterials, *J. Opt.* **14**, 063001 (2012).
- [31] A. V. Kabashin, P. Evans, S. Pastkovsky, W. Hendren, G. A. Wurtz, R. Atkinson, R. Pollard, V. A. Podolskiy, and A. V. Zayats, Plasmonic nanorod metamaterials for biosensing, *Nat. Mater.* **8**, 867 (2009).
- [32] Efthymios Kallos, Ioannis Chremmos, and Vassilios Yannopapas, Resonance properties of optical all-dielectric metamaterials using two-dimensional multipole expansion, *Phys. Rev. B* **86**, 245108 (2012).
- [33] Diana Strickland, Arturo Ayón, and Andrea Alù, Dynamic polarizability tensor for circular cylinders, *Phys. Rev. B* **91**, 085104 (2015).
- [34] Roger E. Raab, Owen L. De Lange, and Owen L. de Lange, *Multipole Theory in Electromagnetism: Classical, Quantum, and Symmetry Aspects, with Applications* (Oxford University Press on Demand, Oxford, United Kingdom, 2005), Vol. 128.
- [35] Laurence D. Barron, *Molecular Light Scattering and Optical Activity* (Cambridge University Press, Cambridge, United Kingdom, 2009).
- [36] Jihua Zhang, Ran Wei, and Chunlei Guo, Simultaneous implementation of antireflection and antitransmission through multipolar interference in plasmonic metasurfaces and applications in optical absorbers and broadband polarizers, *Nanophotonics* **1**, 4529 (2020).
- [37] Boris S. Luk'yanchuk, Nikolai V. Voshchinnikov, Ramón Paniagua-Domínguez, and Arseniy I. Kuznetsov, Optimum forward light scattering by spherical and spheroidal dielectric nanoparticles with high refractive index, *ACS Photonics* **2**, 993 (2015).
- [38] Steven Person, Manish Jain, Zachary Lapin, Juan Jose Sáenz, Gary Wicks, and Lukas Novotny, Demonstration of zero optical backscattering from single nanoparticles, *Nano Lett.* **13**, 1806 (2013).
- [39] Isabelle Staude, Andrey E. Miroshnichenko, Manuel Decker, Nche T. Fofang, Sheng Liu, Edward Gonzales, Jason Dominguez, Ting Shan Luk, Dragomir N. Neshev, Igal Brener, *et al.*, Tailoring directional scattering through magnetic and electric resonances in subwavelength silicon nanodisks, *ACS Nano* **7**, 7824 (2013).
- [40] Debabrata Sikdar, Wenlong Cheng, and Malin Premaratne, Optically resonant magneto-electric cubic nanoantennas for ultra-directional light scattering, *J. Appl. Phys.* **117**, 083101 (2015).
- [41] Viktoriia E. Babicheva and Andrey B. Evlyukhin, Analytical model of resonant electromagnetic dipole-quadrupole

- coupling in nanoparticle arrays, *Phys. Rev. B* **99**, 195444 (2019).
- [42] Laura Pulido-Mancera, Patrick T. Bowen, Mohammadreza F. Imani, Nathan Kundtz, and David Smith, Polarizability extraction of complementary metamaterial elements in waveguides for aperture modeling, *Phys. Rev. B* **96**, 235402 (2017).
- [43] Alexandre Silva, Francesco Monticone, Giuseppe Castaldi, Vincenzo Galdi, Andrea Alù, and Nader Engheta, Performing mathematical operations with metamaterials, *Science* **343**, 160 (2014).
- [44] Farzad Zangeneh-Nejad, Dimitrios L. Sounas, Andrea Alù, and Romain Fleury, Analogue computing with metamaterials, *Nat. Rev. Mater.* **1** (2020).
- [45] You Zhou, Hanyu Zheng, Ivan I. Kravchenko, and Jason Valentine, Flat optics for image differentiation, *Nat. Photonics* **14**, 316 (2020).
- [46] Amirhossein Babaei, Ali Momeni, Ali Abdolali, and Romain Fleury, Parallel optical computing based on mimo metasurface processors with asymmetric optical response, [arXiv:2004.02948](https://arxiv.org/abs/2004.02948) (2020).
- [47] Hoyeong Kwon, Dimitrios Sounas, Andrea Cordaro, Albert Polman, and Andrea Alù, Nonlocal Metasurfaces for Optical Signal Processing, *Phys. Rev. Lett.* **121**, 173004 (2018).
- [48] Tengfeng Zhu, Yihan Zhou, Yijie Lou, Hui Ye, Min Qiu, Zhichao Ruan, and Shanhui Fan, Plasmonic computing of spatial differentiation, *Nat. Commun.* **8**, 1 (2017).
- [49] Ali Momeni, Hamid Rajabalipanah, Ali Abdolali, and Karim Achouri, Generalized Optical Signal Processing Based on Multioperator Metasurfaces Synthesized by Susceptibility Tensors, *Phys. Rev. Appl.* **11**, 064042 (2019).
- [50] Ali Abdolali, Ali Momeni, Hamid Rajabalipanah, and Karim Achouri, Parallel integro-differential equation solving via multi-channel reciprocal bianisotropic metasurface augmented by normal susceptibilities, *New J. Phys.* **21**, 113048 (2019).
- [51] Andrea Cordaro, Hoyeong Kwon, Dimitrios Sounas, A. Femius Koenderink, Andrea Alù, and Albert Polman, High-index dielectric metasurfaces performing mathematical operations, *Nano Lett.* **19**, 8418 (2019).
- [52] Shanshan He, Junxiao Zhou, Shizhen Chen, Weixing Shu, Hailu Luo, and Shuangchun Wen, Spatial differential operation and edge detection based on the geometric spin hall effect of light, *Opt. Lett.* **45**, 877 (2020).
- [53] Tengfeng Zhu, Yijie Lou, Yihan Zhou, Jiahao Zhang, Junyi Huang, Yan Li, Hailu Luo, Shuangchun Wen, Shiyao Zhu, Qihuang Gong, *et al.*, Generalized Spatial Differentiation from the Spin Hall Effect of Light and its Application in Image Processing of Edge Detection, *Phys. Rev. Appl.* **11**, 034043 (2019).
- [54] Hoyeong Kwon, Andrea Cordaro, Dimitrios Sounas, Albert Polman, and Andrea Alu, Dual-polarization analog 2d image processing with nonlocal metasurfaces, *ACS Photonics* **7**, 1799 (2020).
- [55] Yijie Lou, Yisheng Fang, and Zhichao Ruan, Optical computation of divergence operation for vector field, [arXiv:2003.10649](https://arxiv.org/abs/2003.10649) (2020).
- [56] Anders Pors, Michael G. Nielsen, and Sergey I. Bozhevolnyi, Analog computing using reflective plasmonic metasurfaces, *Nano Lett.* **15**, 791 (2015).
- [57] Farzad Zangeneh-Nejad and Romain Fleury, Topological analog signal processing, *Nat. Commun.* **10**, 1 (2019).
- [58] Cheng Guo, Meng Xiao, Momchil Minkov, Yu Shi, and Shanhui Fan, Photonic crystal slab laplace operator for image differentiation, *Optica* **5**, 251 (2018).
- [59] Yi Zhou, Wenhui Wu, Rui Chen, Wenjie Chen, Ruipin Chen, and Yungui Ma, Analog optical spatial differentiators based on dielectric metasurfaces, *Adv. Opt. Mater.* **8**, 1901523 (2020).
- [60] Ali Momeni, Hamid Rajabalipanah, Mahdi Rahmzadeh, Ali Abdolali, Karim Achouri, Viktor Asadchy, and Romain Fleury, Reciprocal metasurfaces for on-axis reflective optical computing, [arXiv:2012.12120](https://arxiv.org/abs/2012.12120) (2020).
- [61] Suhandoko D. Isro, Alexander A. Iskandar, Yuri S. Kivshar, and Ilya V. Shadrivov, Engineering scattering patterns with asymmetric dielectric nanorods, *Opt. Express* **26**, 32624 (2018).
- [62] T. J. Davis, F. Eftekhari, D. E. Gómez, and A. Roberts, Metasurfaces with Asymmetric Optical Transfer Functions for Optical Signal Processing, *Phys. Rev. Lett.* **123**, 013901 (2019).
- [63] L. Klinkenbusch, Two-dimensional scattering of a plane wave by a finite wedge, *Arch. Elektrotechnik* **75**, 261 (1992).
- [64] Saïd Zouhdi, Ari Sihvola, and Alexey P. Vinogradov, *Metamaterials and Plasmonics: Fundamentals, Modelling, Applications* (Springer Science & Business Media, Dordrecht, the Netherlands, 2008).
- [65] Charles Herach Papas, *Theory of Electromagnetic Wave Propagation* (Courier Corporation, New York, 2014).
- [66] Viktor S. Asadchy, Igar A. Faniayeu, Younes Ra'di, and Sergei A. Tretyakov, Determining polarizability tensors for an arbitrary small electromagnetic scatterer, *Photonics Nanostructures-Fundamentals Appl.* **12**, 298 (2014).
- [67] Mohammad Yazdi and Nader Komjani, Polarizability calculation of arbitrary individual scatterers, scatterers in arrays, and substrated scatterers, *JOSA B* **33**, 491 (2016).
- [68] Collin Ladd, Ju-Hee So, John Muth, and Michael D. Dickey, 3d printing of free standing liquid metal microstructures, *Adv. Mater.* **25**, 5081 (2013).
- [69] Jeffrey S. Fisher, Peter A. Kottke, Songkil Kim, and Andrei G. Fedorov, Rapid electron beam writing of topologically complex 3d nanostructures using liquid phase precursor, *Nano Lett.* **15**, 8385 (2015).
- [70] Jie Lian, Lumin Wang, Xiangcheng Sun, Qingkai Yu, and Rodney C. Ewing, Patterning metallic nanostructures by ion-beam-induced dewetting and rayleigh instability, *Nano Lett.* **6**, 1047 (2006).
- [71] Qi Zhang, Yih Hong Lee, In Yee Phang, Choon Keong Lee, and Xing Yi Ling, Hierarchical 3d sers substrates fabricated by integrating photolithographic microstructures and self-assembly of silver nanoparticles, *Small* **10**, 2703 (2014).
- [72] Jincheng Ni, Chaowei Wang, Chenchu Zhang, Yanlei Hu, Liang Yang, Zhaoxin Lao, Bing Xu, Jiawen Li, Dong Wu, and Jiaru Chu, Three-dimensional chiral microstructures fabricated by structured optical vortices in isotropic material, *Light: Sci. Appl.* **6**, e17011 (2017).

- [73] M. S. Mirmoosa, Y. Ra'di, V. S. Asadchy, C. R. Simovski, and S. A. Tretyakov, Polarizabilities of Nonreciprocal Bianisotropic Particles, *Phys. Rev. Appl.* **1**, 034005 (2014).
- [74] Mohammad Yazdi and Nader Komjani, Polarizability tensor calculation using induced charge and current distributions, *Prog. Electromagnetics Res.* **45**, 123 (2016).
- [75] Basab B. Dasgupta and Ronald Fuchs, Polarizability of a small sphere including nonlocal effects, *Phys. Rev. B* **24**, 554 (1981).
- [76] M. Safari, M. Albooyeh, C. R. Simovski, and S. A. Tretyakov, Shadow-free multimers as extreme-performance meta-atoms, *Phys. Rev. B* **97**, 085412 (2018).
- [77] Andrea Alu and Nader Engheta, How does zero forward-scattering in magnetodielectric nanoparticles comply with the optical theorem? *J. Nanophotonics* **4**, 041590 (2010).
- [78] Alexandra Boltasseva, Valentyn S. Volkov, Rasmus B. Nielsen, Esteban Moreno, Sergio G. Rodrigo, and Sergey I. Bozhevolnyi, Triangular metal wedges for subwavelength plasmon-polariton guiding at telecom wavelengths, *Opt. Express* **16**, 5252 (2008).
- [79] Ido Cooperstein, S. R. K. Chaitanya Indukuri, Alisa Bouketov, Uriel Levy, and Shlomo Magdassi, 3d printing of micrometer-sized transparent ceramics with on-demand optical-gain properties, *Adv. Mater.* **32**, 2001675 (2020).
- [80] Amirhossein Babaei, Ali Momeni, Mohammad Moein Moeini, Romain Fleury, and Ali Abdolali, in *2020 Fourteenth International Congress on Artificial Materials for Novel Wave Phenomena (Metamaterials)* (IEEE, New York), p. 195.
- [81] Edward D. Palik, *Handbook of Optical Constants of Solids* (Academic Press, San Diego, California, 1998), Vol. 3.
- [82] M. Albooyeh, D.-H. Kwon, F. Capolino, and S. A. Tretyakov, Equivalent realizations of reciprocal metasurfaces: Role of tangential and normal polarization, *Phys. Rev. B* **95**, 115435 (2017).
- [83] Teemu Niemi, Antti O. Karilainen, and Sergei A. Tretyakov, Synthesis of polarization transformers, *IEEE Trans. Antennas Propag.* **61**, 3102 (2013).